

---

# SELF-SUPERVISED PRE-TRAINING WITH DIFFUSION MODEL FOR FEW-SHOT LANDMARK DETECTION IN X-RAY IMAGES

---

**Roberto Di Via**  
MaLGa, DIBRIS  
University of Genoa  
Via Dodecaneso 35, 16129, Genoa, Italy  
roberto.divia@edu.unige.it

**Francesca Odone**  
MaLGa, DIBRIS  
University of Genoa  
Via Dodecaneso 35, 16129, Genoa, Italy  
francesca.odone@unige.it

**Vito Paolo Pastore**  
MaLGa, DIBRIS  
University of Genoa  
Via Dodecaneso 35, 16129, Genoa, Italy  
vito.paolo.pastore@unige.it

October 30, 2024

## ABSTRACT

Deep neural networks have been extensively applied in the medical domain for various tasks, including image classification, segmentation, and landmark detection. However, their application is often hindered by data scarcity, both in terms of available annotations and images. This study introduces a novel application of denoising diffusion probabilistic models (DDPMs) to landmark detection task, specifically addressing the challenge of limited annotated data in x-ray imaging. Our key innovation lies in leveraging DDPMs for self-supervised pre-training in landmark detection, a previously unexplored approach in this domain. This method enables accurate landmark detection with minimal annotated training data (as few as 50 images), surpassing both ImageNet supervised pre-training and traditional self-supervised techniques across three popular x-ray benchmark datasets. To our knowledge, this work represents the first application of diffusion models for self-supervised learning in landmark detection, which may offer a valuable pre-training approach in few-shot regimes, for mitigating data scarcity.

## 1 Introduction

Landmark detection, the task of identifying anatomical keypoints in images [1], plays a crucial role in various medical applications, including angle measurements [2], skeletal assessments [3], and surgical planning [4]. Although deep neural networks have become prevalent in this domain [5, 6], and many fully supervised methods have been proposed [7, 8, 9, 10, 11, 12, 13, 14, 15], their effectiveness is often limited by the scarcity of annotated data, particularly in medical imaging where expert annotations are costly and time consuming [8, 7, 9]. Consequently, real-world datasets typically contain very few annotated images, requiring the design of label-efficient training solutions [16].

To address this challenge, researchers have explored transfer learning approaches, typically fine-tuning ImageNet pre-trained models on medical tasks [17, 18, 19]. However, the efficacy of in-domain pre-training remains a subject of debate, with recent studies yielding conflicting results across different tasks and domains [20, 9]. Self-supervised learning (SSL) methods such as MoCoV3 [21], SimCLRv2 [22], and DINO [23] have emerged as promising alternatives, enabling models to learn robust representations from unlabeled data. These approaches have shown potential to reduce the dependency on large labeled datasets, especially for medical imaging applications.

In this context, our primary contribution lies in the novel application of DDPM to the task of landmark detection in x-ray images. While DDPMs have demonstrated remarkable success in image generation tasks [24, 25], their potential for

self-supervised pre-training in medical image analysis, particularly landmark detection, remains largely unexplored. We propose a few-shot self-supervised pre-training approach specifically tailored for landmark detection in x-ray images, widely used for anatomical assessment and diagnosis, addressing the realistic and typical scenario where the available annotations and images are minimal (up to 50).

To our knowledge, this work represents the first application of diffusion models for self-supervision in landmark detection. We conduct a comprehensive comparison of our method against state-of-the-art alternatives, including YOLO [8], ImageNet supervised pre-training and self-supervised approaches like MoCoV3, SimCLRv2, and DINO. Our evaluation focuses on performance and robustness across varying quantities of labeled training samples.

Our results demonstrate that our DDPM-based approach outperforms both ImageNet supervised pre-training and other self-supervised methods in the landmark detection task. Furthermore, we perform a set of experiments to provide insights on whether the usage of a different in-domain pre-training dataset may benefit the downstream task, in a few shot regimes.

This work not only introduces a novel application of DDPMs for the landmark detection task but also contributes to the ongoing discussion on effective pre-training strategies for medical imaging tasks with limited annotations.

The remainder of the paper is organized as follows: Section 2 reviews related studies, particularly focusing on self-supervised pre-training in the medical domain and landmark detection. Section 3 describes our proposed approach. Section 4 gives an overview of the benchmark datasets employed in this research and explains the evaluation metrics. Lastly, Section 5 showcases our experimental results and insights, drawing some conclusions in Section 6.

## 2 Related Works

Few-shot learning is particularly relevant in medical applications due to the high cost and time-intensive nature of obtaining high-quality, unbiased annotations [26]. To address this challenge, researchers have explored various approaches, with transfer learning and self-supervised learning emerging as two prominent strategies.

Building upon these advancements in both self-supervised learning and diffusion models, our work distinguishes itself by examining the impact of self-supervised pre-training with diffusion models on landmark detection for x-ray images in a realistic scenario with limited annotations and images, a common challenge in medical imaging.

To our knowledge, this study represents the first application of diffusion models for self-supervised learning in the specific task of landmark detection in x-ray images. This novel approach bridges the gap between the established potential of diffusion models in other medical imaging tasks and the pressing need for label-efficient methods in landmark detection.

## 3 Approach

Fig. 1 illustrates our two-step methodology: initially, a DDPM is pre-trained on the training set, in a self-supervised fashion (with no annotations). Subsequently, this model is fine-tuned on the labeled training set for the downstream task, represented by the landmark detection. Further details on these steps are discussed below.

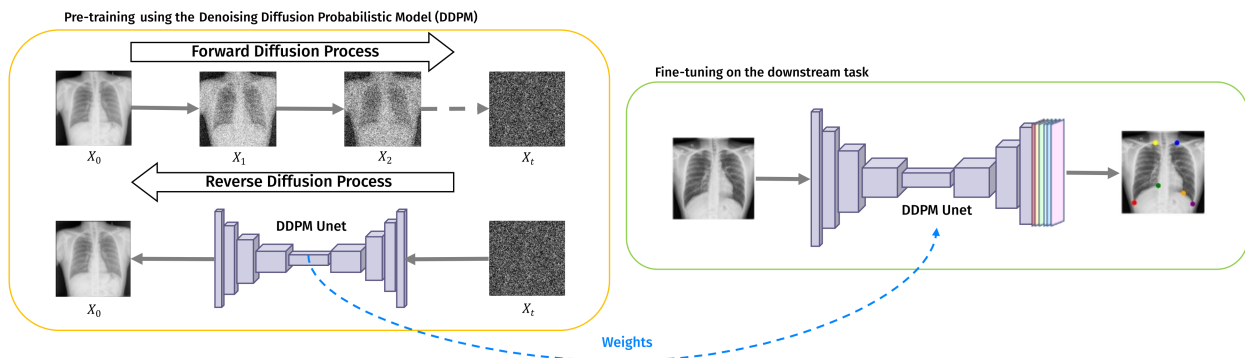


Figure 1: Schematic representation of our DDPM self-supervised landmark detection pipeline.

**DDPMs background.** Denoising Diffusion Probabilistic Models (DDPMs) [27] have emerged as a powerful class of generative models, excelling in the synthesis of high-fidelity samples in diverse fields, including medical imaging [24, 25]. DDPMs comprise two key processes: forward diffusion and reverse diffusion.

### 1. Forward Diffusion Process:

The forward diffusion process is described by:

$$q(x_t|x_{t-1}) = \mathcal{N}(x_t; \sqrt{1 - \beta_t}x_{t-1}, \beta_t\mathbf{I}) \quad (1)$$

Here,  $q(x_t|x_{t-1})$  represents the probability distribution of  $x_t$  given  $x_{t-1}$ .  $\mathcal{N}$  denotes a Gaussian distribution with mean  $\sqrt{1 - \beta_t}x_{t-1}$  and variance  $\beta_t\mathbf{I}$ .  $\beta_t$  is a variance schedule that increases with  $t$ , controlling the amount of noise added at each step.  $\mathbf{I}$  is the identity matrix. The process can be expressed as a single step:

$$q(x_t|x_0) = \mathcal{N}(x_t; \sqrt{\bar{\alpha}_t}x_0, (1 - \bar{\alpha}_t)\mathbf{I}) \quad (2)$$

where  $\bar{\alpha}_t = \prod_{s=1}^t(1 - \beta_s)$ . This equation allows direct sampling of  $x_t$  given  $x_0$ , with  $\sqrt{\bar{\alpha}_t}x_0$  as the mean and  $(1 - \bar{\alpha}_t)\mathbf{I}$  as the variance.

### 2. Reverse Diffusion Process:

The reverse diffusion process is modeled as:

$$p_\theta(x_{t-1}|x_t) = \mathcal{N}(x_{t-1}; \mu_\theta(x_t, t), \Sigma_\theta(x_t, t)) \quad (3)$$

Here,  $p_\theta(x_{t-1}|x_t)$  is the probability of  $x_{t-1}$  given  $x_t$ .  $\mu_\theta(x_t, t)$  and  $\Sigma_\theta(x_t, t)$  are the mean and covariance predicted by a neural network with parameters  $\theta$ . The mean of the reverse process is estimated by:

$$\mu_\theta(x_t, t) = \frac{1}{\sqrt{\alpha_t}} \left( x_t - \frac{\beta_t}{\sqrt{1 - \bar{\alpha}_t}} \epsilon_\theta(x_t, t) \right) \quad (4)$$

where  $\epsilon_\theta(x_t, t)$  is the noise predicted by the neural network. The terms  $\frac{1}{\sqrt{\alpha_t}}$  and  $\frac{\beta_t}{\sqrt{1 - \bar{\alpha}_t}}$  are scaling factors that adjust for the noise level at time  $t$ .

The training objective is:

$$\mathcal{L}_{\text{simple}} = \mathbb{E}_{t, x_0, \epsilon} [\|\epsilon - \epsilon_\theta(\sqrt{\bar{\alpha}_t}x_0 + \sqrt{1 - \bar{\alpha}_t}\epsilon, t)\|^2] \quad (5)$$

This loss function trains the model to predict the noise  $\epsilon$  added at each timestep.  $\epsilon_\theta(\cdot)$  is the noise predicted by the model, and  $\sqrt{\bar{\alpha}_t}x_0 + \sqrt{1 - \bar{\alpha}_t}\epsilon$  is the noisy input to the model at time  $t$ . The expectation  $\mathbb{E}_{t, x_0, \epsilon}$  is taken over random timesteps, images, and noise samples.

**Pre-training using the DDPM.** In this work, we leverage a DDPM U-Net architecture as a pre-training strategy for anatomical landmark detection using unannotated medical images. This approach captures multi-scale anatomical representations, with DDPM’s denoising process extracting features at various levels and U-Net’s skip connections preserving both fine details and global information. During pre-training, the model learns to generate new images with the same pixel distribution as the originals, enabling it to learn important anatomical features.

Given the typical scarcity of labeled data in real-world landmark detection, our DDPM U-Net is designed for effective pre-training on small-scale unannotated datasets while maintaining computational efficiency and minimizing training time. This approach yields rich and general features for the downstream task, offering an effective few-shot learning framework for landmark detection. By leveraging unannotated medical data, our model develops a comprehensive understanding of anatomical structures, creating a robust foundation that can adapt to specific landmark detection tasks with minimal additional training.

**Ground-truth heatmaps generation.** We formulate landmark detection as a classification problem over all image pixels to generate output heatmaps. This approach enables simultaneous prediction of multiple landmarks, with one heatmap per landmark. Specifically, our model outputs  $N$  heatmaps, where  $N$  is the number of landmarks to predict. For heatmap generation, we adopt a Gaussian-based approach inspired by [8]. This strategy involves applying a Gaussian filter ( $\sigma = 5$ ) centered at the ground-truth landmark location, followed by thresholding to obtain binary images. Formally:

$$H_g(i, j) = \begin{cases} 1, & \text{if } \exp\left(-\frac{(i-x)^2 + (j-y)^2}{2\sigma^2}\right) > \frac{1}{2} \max(G) \\ 0, & \text{otherwise} \end{cases}$$

Where  $H_g(i, j)$  is the Gaussian heatmap pixel value at  $(i, j)$ ,  $(x, y)$  are the ground truth landmark coordinates, and  $G$  is the Gaussian-filtered image before thresholding.

Training on these heatmaps enables our model to learn landmark spatial relationships, predicting both general areas of interest and precise coordinates, and potentially enhance downstream landmark detection.

**Fine-tuning on the downstream task.** The pre-trained DDPM UNet model is adapted for anatomical landmark detection, bridging the gap between generative modeling and precise anatomical localization. This adaptation, illustrated in Figure 1, involves a subtle yet powerful modification of the UNet architecture. While preserving the core structure that proved so effective in the DDPM, we alter the final convolutional layer to output multiple channels (each corresponding to a predicted heatmap for a specific anatomical landmark) and the timestep embedding is set to be null (as the temporal aspect is irrelevant for static landmark detection). This architectural shift transforms the model from a general image generator to a specialized landmark detector, capitalizing on learned hierarchical representations.

Our fine-tuning strategy transitions from DDPM’s self-supervised paradigm to a supervised approach tailored for landmark detection. Training with ground-truth heatmaps allows the model to repurpose its learned features for precise spatial localization. Landmark coordinates are derived by calculating the centroid of each heatmap generated.

This supervised fine-tuning, combined with pre-trained weight transfer (indicated by the blue dashed arrow), enables quick adaptation to the new task with minimal annotated data. The approach’s efficacy in few-shot learning contexts highlights its potential for medical imaging applications, where large annotated datasets are often scarce. By harnessing the power of diffusion models, traditionally used for generation tasks, we show their unexplored potential in discriminative tasks like landmark detection.

## 4 Experimental Setup

### 4.1 Datasets and Evaluation Metrics

We evaluate our method on three public x-ray datasets standard in landmark detection research, following the dataset splits and evaluation protocols of [8, 9]. The **Chest x-ray dataset** [28] comprises 279 images (approximately 3000×3000 pixels, resolution unknown) with 6 landmarks, split into 195 for training, 34 for validation, and 50 for testing. The **Cephalometric x-ray dataset** [29] consists of 400 lateral cephalograms (2400×1935 pixels, 0.1 mm resolution) with 19 target landmarks, split into 130 for training, 20 for validation, and 250 for testing. The **Hand x-ray dataset** [30] contains 909 radiographs (average size 1563×2169 pixels) with 37 labeled landmarks, assuming a 50 mm length between wrist endpoints [31], split into 550 for training, 59 for validation, and 300 for testing.

Our model is assessed using two standard metrics [26, 32]: the *mean radial error* (MRE) and the *successful detection rate* (SDR). MRE measures the Euclidean distance between predicted and ground truth landmarks, while SDR calculates the percentage of predictions within dataset-specific thresholds. For the Chest dataset, we report these metrics in pixels due to unavailable physical spacing information, whereas for Cephalometric and Hand datasets, we use millimeters, adhering to field standards.

### 4.2 Implementation Details

The experiments are conducted on a single NVIDIA A30 GPU with 24 GB RAM, using Python 3.10 and PyTorch 2.1.0. For data pre-processing, images are resized to 256x256 pixels, normalized to  $[0 - 1]$  range, and augmented during training with random rotations ( $-2^\circ$  and  $2^\circ$ ), scaling ( $-0.02$  to  $0.02$ ), and translations ( $-0.02$  to  $0.02$ ).

**Pre-training stage.** The DDPM is trained with a batch size of 4, with gradient accumulation every 8 batches. Training involves 500 diffusion steps with a linear noise schedule. The training process spans  $10k$  iterations, and we save the weights at iterations  $4k$ ,  $6k$ ,  $8k$ , and  $10k$  for comparison during fine-tuning. We utilize the AdamW optimizer with a learning rate of  $1e^{-4}$  and apply the exponential moving average to model parameters with a decay factor of 0.995. We employ mean squared error as the loss function, consistent with the paper [27].

The DDPM Unet architecture features a multi-scale approach with channel multipliers [1, 2, 4, 8], indicating the increase in channels at each down-sampling stage. It incorporates attention mechanisms at a resolution of 32, uses 4 attention heads per channel, and includes 4 residual blocks at each resolution level.

Concerning the implementation of other SSL and ImageNet pre-training techniques, the sources are [33] and [34].

**Fine-tuning stage.** The fine-tuning process is carried out using the AdamW optimizer for 200 epochs, with

an early stopping criterion. The learning rate is adjusted using a ReduceLROnPlateau scheduler based on the validation loss, starting at an initial value of  $1e^{-5}$ . The batch size is set at 2, with a gradient accumulation of 8. We use cross-entropy loss for gaussian heatmaps, and a negative log-likelihood loss for the contour-hugging ones [35].

## 5 Experimental Results

### 5.1 Tuning the DDPM pre-training iterations

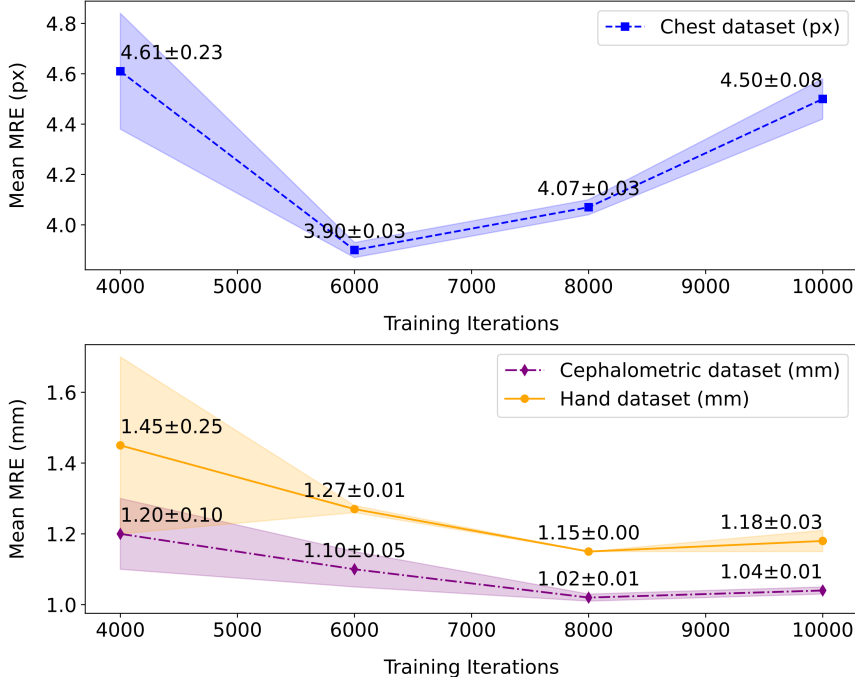


Figure 2: Landmark detection performance on Chest, Cephalometric, and Hand validation sets across DDPM pre-training iterations.

The number of training iterations during DDPM pre-training is a fundamental hyperparameter in our approach. To evaluate its impact and determine the optimal value, we conducted an experiment running the entire pipeline three times, considering  $4k$ ,  $6k$ ,  $8k$ , and  $10k$  iterations for the DDPM pre-training step. Figure 2 illustrates the landmark detection results obtained on the validation sets for the Chest, Cephalometric, and Hand datasets in terms of MRE.

Our findings indicate that the pre-training is quite robust, except for the  $4k$  iterations where the model is likely still learning crucial data features (as shown by the high standard deviation). Excessive training iterations beyond  $8k$  may result in overfitting, resulting in slightly degraded performance on the downstream task. Based on these results, we selected the optimal number of training iterations for DDPM pre-training in subsequent experiments, utilizing  $6k$ ,  $8k$ , and  $8k$  iterations for the Chest, Cephalometric, and Hand datasets respectively.

### 5.2 Downstream task performance evaluation

We assess the effectiveness of our DDPM self-supervised pre-training method by benchmarking it against supervised ImageNet pre-training and self-supervised state-of-the-art methods (MoCoV3, SimCLRv2, and DINO) across different numbers of labeled training samples (1, 5, 10, 25, and 50) in the Chest, Cephalometric, and Hand datasets. Additionally, we explore an ablation of our method using the contour-hugging approach [35] as an alternative framework for the downstream task. Tables 1, 2, and 3 report the average test results for three independent runs (a bar chart version of the tables is provided in the Supplementary Material). Except for our approach, which implements a DDPM as described in [27], all methods use DenseNet161 as the encoder backbone, chosen for its performance across all datasets based on hold-out validation comparisons with VGG19 and ResNeXt50\_32x4D.

Our approach consistently outperforms both ImageNet and alternative SSL approaches across all datasets and training image quantities. Figure 3 provides visual support, showing prediction heatmaps for each method with 10 labels across

all datasets. Performance gains are particularly pronounced in low-data regimes. For instance, in the Chest dataset (Table 1) with one labeled sample, our method achieves an MRE of 14.99px compared to 143.67px for ImageNet and 64.69px for DINO (the best alternative), representing reductions of 89.6% and 76.8% respectively. The SDR at 9px shows even greater improvements, with our method reaching 64.63%, far surpassing other approaches.

Table 1: Comparing landmark detection test performance on the Chest dataset through our DDPM self-supervised pre-training and ImageNet, MoCoV3, SimCLRv2, DINO pre-training across varying numbers of labeled training images, highlighting best results in bold.

Number of Labeled Training Samples	Pre-trained Models	Chest			
		MRE ↓ (px)	SDR(%) ↑		
			3px	6px	9px
1	ImageNet	143.67 ± 0.27	0.00 ± 0.00	0.00 ± 0.00	0.00 ± 0.00
	MoCoV3	106.74 ± 14.95	2.98 ± 0.51	12.33 ± 2.26	19.92 ± 3.47
	SimCLRv2	118.97 ± 1.84	1.90 ± 0.19	6.09 ± 0.58	11.39 ± 0.58
	DINO	64.69 ± 0.91	3.66 ± 0.33	15.72 ± 0.38	23.44 ± 0.38
	Our method with [35]	50.03 ± 0.00	<b>21.14 ± 0.00</b>	43.90 ± 0.00	50.81 ± 0.00
	Our method	<b>14.99 ± 0.00</b>	19.92 ± 0.00	<b>46.34 ± 0.00</b>	<b>64.63 ± 0.00</b>
5	ImageNet	72.81 ± 2.71	2.44 ± 0.33	8.54 ± 1.00	14.09 ± 1.38
	MoCoV3	18.35 ± 0.18	14.63 ± 1.00	41.60 ± 0.69	66.53 ± 0.69
	SimCLRv2	30.09 ± 0.35	15.72 ± 0.69	48.37 ± 1.45	67.48 ± 0.33
	DINO	24.48 ± 1.73	11.25 ± 1.16	32.65 ± 0.51	48.78 ± 1.00
	Our method with [35]	8.14 ± 0.00	<b>60.16 ± 0.00</b>	<b>82.11 ± 0.00</b>	<b>86.99 ± 0.00</b>
	Our method	<b>6.04 ± 0.00</b>	32.52 ± 0.00	65.04 ± 0.00	<b>86.99 ± 0.00</b>
10	ImageNet	35.83 ± 1.57	7.11 ± 0.84	22.56 ± 1.06	37.30 ± 1.39
	MoCoV3	13.52 ± 0.67	18.49 ± 0.21	44.72 ± 1.21	67.28 ± 1.43
	SimCLRv2	28.50 ± 0.00	17.89 ± 0.00	45.93 ± 0.00	64.63 ± 0.00
	DINO	14.96 ± 0.03	16.26 ± 0.41	39.64 ± 0.21	61.99 ± 0.61
	Our method with [35]	<b>4.47 ± 0.00</b>	<b>60.98 ± 0.00</b>	<b>88.62 ± 0.00</b>	<b>93.50 ± 0.00</b>
	Our method	5.33 ± 0.00	33.74 ± 0.00	67.89 ± 0.00	86.59 ± 0.00
25	ImageNet	11.38 ± 1.11	20.83 ± 2.00	49.29 ± 1.13	70.33 ± 0.29
	MoCoV3	6.15 ± 0.00	30.89 ± 0.00	66.67 ± 0.00	85.37 ± 0.00
	SimCLRv2	11.46 ± 0.00	33.74 ± 0.00	69.11 ± 0.00	84.15 ± 0.00
	DINO	10.32 ± 0.35	24.59 ± 1.02	55.69 ± 0.81	75.81 ± 0.20
	Our method with [35]	<b>2.92 ± 0.00</b>	<b>76.02 ± 0.00</b>	<b>94.31 ± 0.00</b>	<b>96.34 ± 0.00</b>
	Our method	4.62 ± 0.00	32.93 ± 0.00	73.17 ± 0.00	91.87 ± 0.00
50	ImageNet	7.36 ± 0.31	29.98 ± 1.73	67.58 ± 2.45	83.23 ± 0.34
	MoCoV3	4.42 ± 0.00	39.43 ± 0.00	77.64 ± 0.00	92.68 ± 0.00
	SimCLRv2	7.93 ± 0.00	37.40 ± 0.00	73.98 ± 0.00	91.87 ± 0.00
	DINO	7.62 ± 1.04	30.89 ± 1.22	62.81 ± 1.43	82.32 ± 3.05
	Our method with [35]	<b>2.69 ± 0.00</b>	<b>76.83 ± 0.00</b>	<b>93.50 ± 0.00</b>	<b>97.56 ± 0.00</b>
	Our method	4.31 ± 0.01	39.63 ± 0.61	80.08 ± 0.41	93.50 ± 0.41

Similar trends are observed in the Cephalometric (Table 2) and Hand datasets (Table 3). With one labeled sample in the Cephalometric dataset, our method attains an MRE of 15.71mm versus 86.71mm for ImageNet and 43.49mm for MoCoV3, with corresponding improvements in SDR. In the Hand dataset, our approach yields an MRE of 28.75mm versus 79.32mm for ImageNet and 97.31mm for DINO, again with SDR improvements. As the number of labeled samples increases, the performance gap narrows, though our approach maintains an edge. For example, in the Cephalometric dataset with 25 labeled samples, our method’s MRE of 2.84mm still outperforms ImageNet’s 7.67mm and SimCLRv2’s 3.99mm. This trend is consistent across all datasets, indicating that our method provides substantial benefits in extremely low-data scenarios while continuing to offer improvements as more labeled data becomes available. These results highlight our DDPM self-supervised pre-training’s effectiveness for landmark detection in few-shot learning scenarios, common in medical imaging where high-quality annotated images are limited.

Finally, to contextualize our results, we compare our method to YOLO [8], a state-of-the-art universal anatomical landmark detection model. YOLO utilizes mixed dataset training and combines a universal U-Net for local feature learning with a global network for landmark disambiguation. As Table 4 shows, our method performs comparably or better than YOLO variants across all three datasets. Despite YOLO’s mixed dataset training (denoted by ‘+’), our approach achieves competitive results with just one labeled sample, even with 5 and 10 samples.

**Ablation study on the downstream task setting.** We perform an ablation study comparing the performance of our downstream task framework, with the one introduced in [35] (second-last entry in our results Tables), mainly differing in the usage of a single annotated pixel to generate unrestricted contour-hugging heatmaps and a negative log-likelihood loss. For the Hand dataset, which had more extensive pre-training data, our approach consistently outperforms the evaluated alternative. However, the contour-hugging method generally shows better SDR performance on the Chest and the Cephalometric datasets. Regarding MRE, our original framework performs better up to 10 training samples, showing lower performance with more annotated data. These findings suggest that the effectiveness of each downstream setting depends on pre-training data volume and quality, as well as dataset-specific characteristics.

Table 2: Comparing landmark detection test performance on Cephalometric dataset through our DDPM self-supervised pre-training and ImageNet, MoCoV3, SimCLRv2, DINO pre-training across varying numbers of labeled training images, highlighting best results in bold.

Number of Labeled Training Samples	Pre-trained Models	MRE ↓ (mm)	Cephalometric SDR(%) ↑			
			2mm	2.5mm	3mm	4mm
1	ImageNet	86.71 ± 0.02	0.02 ± 0.00	0.06 ± 0.00	0.06 ± 0.00	0.15 ± 0.00
	MoCoV3	43.49 ± 1.21	6.79 ± 0.10	10.83 ± 0.25	13.67 ± 0.30	19.99 ± 0.30
	SimCLRv2	100.68 ± 12.18	0.82 ± 0.42	1.27 ± 0.68	1.63 ± 0.79	2.51 ± 1.19
	DINO	58.67 ± 1.22	2.47 ± 0.14	4.42 ± 0.07	5.52 ± 0.07	8.60 ± 0.30
	Our method with [35]	20.13 ± 0.00	<b>18.06 ± 0.00</b>	25.14 ± 0.00	31.94 ± 0.00	41.37 ± 0.00
	Our method	<b>15.71 ± 0.00</b>	17.31 ± 0.00	<b>27.14 ± 0.00</b>	<b>33.24 ± 0.00</b>	<b>45.14 ± 0.00</b>
5	ImageNet	84.40 ± 0.02	0.06 ± 0.00	0.11 ± 0.00	0.15 ± 0.00	0.17 ± 0.00
	MoCoV3	13.44 ± 0.12	18.62 ± 0.19	29.56 ± 0.18	35.99 ± 0.02	49.38 ± 0.16
	SimCLRv2	24.59 ± 0.12	13.06 ± 0.31	21.24 ± 0.25	26.44 ± 0.23	36.52 ± 0.37
	DINO	23.83 ± 0.21	14.00 ± 0.26	23.01 ± 0.54	28.42 ± 0.52	39.13 ± 0.38
	Our method with [35]	11.53 ± 0.00	<b>45.05 ± 0.00</b>	<b>54.00 ± 0.00</b>	<b>61.03 ± 0.00</b>	<b>70.55 ± 0.00</b>
	Our method	<b>8.30 ± 0.00</b>	27.18 ± 0.00	42.65 ± 0.00	51.01 ± 0.00	66.34 ± 0.00
10	ImageNet	50.09 ± 0.44	3.18 ± 0.16	5.92 ± 0.25	7.49 ± 0.26	11.19 ± 0.42
	MoCoV3	9.30 ± 0.03	23.84 ± 0.12	37.20 ± 0.13	45.34 ± 0.17	60.18 ± 0.13
	SimCLRv2	18.54 ± 0.09	17.80 ± 0.29	28.16 ± 0.04	34.65 ± 0.22	46.74 ± 0.23
	DINO	15.64 ± 0.26	18.86 ± 0.12	30.89 ± 0.10	38.22 ± 0.34	51.83 ± 0.45
	Our method with [35]	5.21 ± 0.00	<b>52.11 ± 0.00</b>	<b>62.97 ± 0.00</b>	<b>71.43 ± 0.00</b>	<b>81.68 ± 0.00</b>
	Our method	<b>3.52 ± 0.00</b>	32.06 ± 0.00	48.59 ± 0.00	58.97 ± 0.00	74.69 ± 0.00
25	ImageNet	7.67 ± 0.39	24.25 ± 0.10	37.83 ± 0.13	45.58 ± 0.26	62.56 ± 0.35
	MoCoV3	4.04 ± 0.03	34.81 ± 0.18	51.26 ± 0.14	60.80 ± 0.03	76.78 ± 0.10
	SimCLRv2	3.99 ± 0.04	30.63 ± 0.23	47.04 ± 0.18	56.20 ± 0.13	73.29 ± 0.21
	DINO	5.38 ± 0.19	30.00 ± 0.20	45.98 ± 0.04	55.36 ± 0.06	72.30 ± 0.19
	Our method with [35]	<b>2.72 ± 0.00</b>	<b>65.47 ± 0.00</b>	<b>75.77 ± 0.00</b>	<b>82.55 ± 0.00</b>	<b>90.61 ± 0.00</b>
	Our method	2.84 ± 0.00	39.84 ± 0.01	57.61 ± 0.01	67.17 ± 0.01	81.01 ± 0.00
50	ImageNet	2.82 ± 0.09	42.93 ± 2.66	60.74 ± 3.48	69.69 ± 3.28	83.87 ± 2.24
	MoCoV3	2.98 ± 0.01	43.68 ± 0.32	61.84 ± 0.13	70.48 ± 0.03	84.81 ± 0.19
	SimCLRv2	3.17 ± 0.04	39.94 ± 0.19	58.70 ± 0.08	67.66 ± 0.05	81.85 ± 0.10
	DINO	2.98 ± 0.02	40.33 ± 0.38	59.06 ± 0.39	68.99 ± 0.42	83.78 ± 0.64
	Our method with [35]	<b>2.13 ± 0.00</b>	<b>73.60 ± 0.00</b>	<b>81.22 ± 0.00</b>	<b>86.78 ± 0.00</b>	<b>92.70 ± 0.00</b>
	Our method	2.50 ± 0.00	44.91 ± 0.05	62.84 ± 0.02	72.82 ± 0.00	85.81 ± 0.02

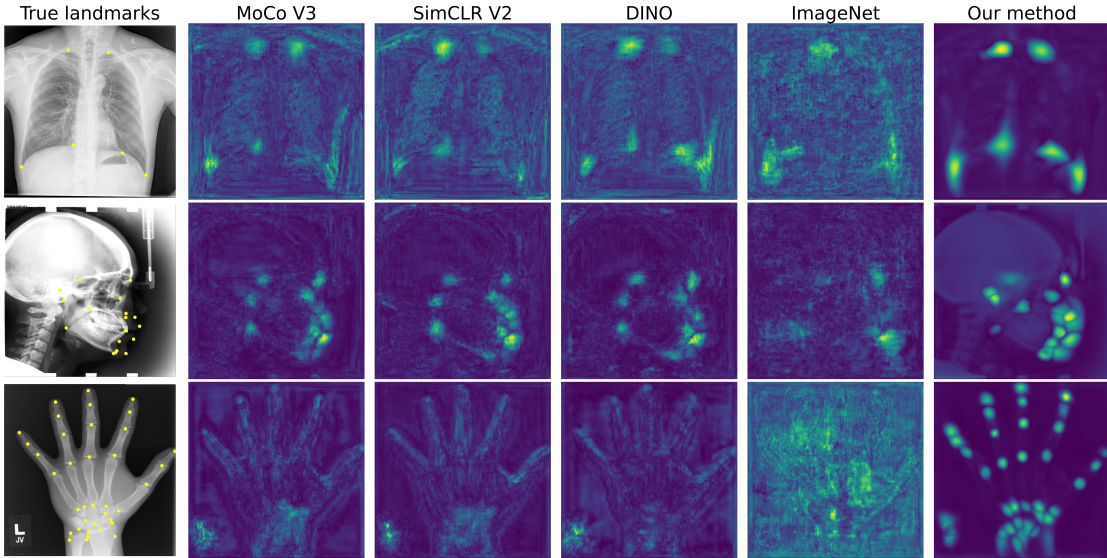


Figure 3: Comparison of landmark detection performance between our DDPM pre-training method and alternative self-supervised and ImageNet pre-training approaches on Chest, Cephalometric, and Hand x-ray test sets, using only 10 labeled training samples.

### 5.3 Impact of different pre-training datasets

In this section, we investigate whether a different in-domain dataset can enhance performance when both available images and annotations are limited. We select the best DDPM model pre-trained on the larger Hand dataset and

Table 3: Comparing landmark detection test performance on the Hand dataset through our DDPM self-supervised pre-training and ImageNet, MoCoV3, SimCLRv2, and DINO pre-training across varying numbers of labeled training images, highlighting best results in bold.

Number of Labeled Training Samples	Pre-trained Models	Hand			
		MRE ↓ (mm)	SDR(%) ↑		
			2mm	4mm	10mm
1	ImageNet	79.32 ± 0.03	0.04 ± 0.00	0.14 ± 0.00	1.08 ± 0.02
	MoCoV3	100.17 ± 0.10	0.42 ± 0.02	0.83 ± 0.02	1.60 ± 0.03
	SimCLRv2	98.52 ± 0.09	0.06 ± 0.01	0.31 ± 0.00	1.02 ± 0.04
	DINO	97.31 ± 0.09	0.47 ± 0.04	1.27 ± 0.03	3.30 ± 0.18
	Our method with [35]	47.76 ± 0.00	8.70 ± 0.00	12.76 ± 0.00	16.59 ± 0.00
	Our method	<b>28.75 ± 0.00</b>	<b>27.87 ± 0.00</b>	<b>46.44 ± 0.00</b>	<b>58.75 ± 0.00</b>
5	ImageNet	86.12 ± 0.03	0.01 ± 0.01	0.09 ± 0.01	1.01 ± 0.01
	MoCoV3	61.20 ± 0.39	9.82 ± 0.16	18.94 ± 0.29	32.11 ± 0.61
	SimCLRv2	75.07 ± 0.48	5.99 ± 0.07	11.87 ± 0.14	20.35 ± 0.34
	DINO	86.03 ± 0.64	2.05 ± 0.31	5.79 ± 0.55	11.96 ± 0.84
	Our method with [35]	37.53 ± 0.00	21.49 ± 0.00	28.90 ± 0.00	34.17 ± 0.00
	Our method	<b>6.86 ± 0.00</b>	<b>61.09 ± 0.00</b>	<b>83.30 ± 0.00</b>	<b>90.62 ± 0.00</b>
10	ImageNet	85.87 ± 0.00	0.01 ± 0.00	0.15 ± 0.00	0.99 ± 0.00
	MoCoV3	55.43 ± 0.29	13.92 ± 0.17	26.00 ± 0.15	40.21 ± 0.20
	SimCLRv2	55.58 ± 0.75	16.72 ± 0.36	29.45 ± 0.45	42.18 ± 0.72
	DINO	60.58 ± 0.53	11.09 ± 0.14	23.00 ± 0.12	35.47 ± 0.32
	Our method with [35]	25.47 ± 0.00	35.67 ± 0.00	45.34 ± 0.00	51.01 ± 0.00
	Our method	<b>4.94 ± 0.11</b>	<b>62.55 ± 0.55</b>	<b>86.08 ± 0.25</b>	<b>94.28 ± 0.17</b>
25	ImageNet	24.96 ± 0.47	42.79 ± 0.60	57.93 ± 0.28	71.68 ± 0.18
	MoCoV3	40.03 ± 0.12	27.19 ± 0.09	44.30 ± 0.27	56.55 ± 0.05
	SimCLRv2	40.02 ± 0.11	29.69 ± 0.06	47.03 ± 0.00	59.73 ± 0.11
	DINO	49.27 ± 0.30	21.09 ± 0.06	36.12 ± 0.10	48.76 ± 0.20
	Our method with [35]	11.99 ± 0.00	62.21 ± 0.00	77.03 ± 0.00	81.39 ± 0.00
	Our method	<b>2.39 ± 0.00</b>	<b>72.99 ± 0.00</b>	<b>93.18 ± 0.00</b>	<b>97.87 ± 0.00</b>
50	ImageNet	10.79 ± 0.23	61.98 ± 0.36	78.51 ± 0.26	90.04 ± 0.28
	MoCoV3	23.77 ± 0.34	47.44 ± 0.10	67.96 ± 0.14	76.18 ± 0.23
	SimCLRv2	23.95 ± 0.18	49.28 ± 0.30	68.56 ± 0.45	77.03 ± 0.69
	DINO	34.95 ± 0.59	34.06 ± 0.97	52.32 ± 1.20	64.21 ± 0.80
	Our method with [35]	7.16 ± 0.00	<b>79.38 ± 0.00</b>	88.36 ± 0.00	90.19 ± 0.00
	Our method	<b>1.74 ± 0.03</b>	78.04 ± 0.94	<b>96.35 ± 0.51</b>	<b>99.02 ± 0.04</b>

Table 4: Comparison of our method vs. state-of-the-art YOLO framework using 1, 5, and 10 labeled samples. + indicates mixed dataset training. Both methods utilizes input images resized at 256x256 pixels. Our method performs competitively using only 1 labeled sample.

Methods	Number of Labeled Training Samples	Chest				Cephalometric				Hand				
		MRE ↓ (px)	SDR(%) ↑			MRE ↓ (mm)	SDR(%) ↑			MRE ↓ (mm)	SDR(%) ↑			
			3px	6px	9px		2mm	2.5mm	3mm		4mm	2mm	4mm	10mm
YOLO+	10	22.55	32.11	63.82	76.42	15.05	18.23	26.50	39.62	53.49	52.43	11.59	19.52	24.14
YOLO+	5	23.13	23.57	50.40	67.07	19.38	11.53	17.07	25.95	35.53	64.24	15.15	24.91	31.79
YOLO+	1	84.37	4.07	13.41	19.51	53.80	7.35	11.22	17.26	23.39	61.36	8.26	17.16	31.47
Our method	1	14.99	19.92	46.34	64.63	15.71	17.31	27.14	33.24	45.14	28.75	27.87	46.44	58.75

fine-tune it on the smaller Chest and Cephalometric datasets, following the same protocol as previous experiments with Gaussian heatmaps. Table 5 reports the results.

Our experiments show the effectiveness of using a larger in-domain dataset (Hand) for pre-training in scenarios with limited target task data. For the Chest landmark detection task, the Hand pre-trained model outperforms the Chest pre-trained model in most scenarios (5 to 50 labeled images). Even with just one labeled sample, it achieves comparable performance to the Chest pre-trained model. For the Cephalometric landmark detection task, while the Hand pre-trained model doesn't surpass the Cephalometric pre-trained model, it achieves competitive results across all training sample quantities. The small performance gap indicates that Hand pre-training still transfers useful features to the Cephalometric task. Notably, our approach consistently outperforms other pre-training methods (ImageNet, MoCoV3, SimCLRv2, DINO) and frameworks (YOLO) for both tasks, regardless of the number of labeled training samples. This underscores the value of in-domain pre-training using our approach, even when the pre-training dataset differs from the target task.

Our goal is to simulate real-world scenarios with limited data and label availability by utilizing images from the same dataset as the downstream task. We focused on label-efficient pre-training while minimizing computational resource usage, given the substantial resources and time required for training diffusion models on extensive unlabeled datasets. While larger unlabeled datasets might enhance pre-training outcomes, our key finding is that using a limited unannotated



Table 5: Landmark detection test performance of our Gaussian-heatmaps method, pre-trained on the Hand dataset and fine-tuned on the Chest / Cephalometric datasets, across varying numbers of labeled training images.

Number of Labeled Training Samples	Hand pre-training → Chest fine-tuning				Hand pre-training → Cephalometric fine-tuning				
	MRE±STD ↓ (px)	SDR(%)±STD ↑			MRE±STD ↓ (mm)	SDR(%)±STD ↑			
		3px	6px	9px		2mm	2.5mm	3mm	4mm
1	23.79 ± 0.00	14.23 ± 0.00	35.37 ± 0.00	52.03 ± 0.00	9.56 ± 0.28	30.45 ± 1.73	38.60 ± 1.78	47.75 ± 2.00	60.21 ± 1.73
5	5.86 ± 0.00	32.93 ± 0.00	65.04 ± 0.00	82.93 ± 0.00	5.42 ± 0.00	55.07 ± 0.00	64.55 ± 0.00	72.44 ± 0.00	79.71 ± 0.00
10	5.08 ± 0.00	34.55 ± 0.00	70.73 ± 0.00	85.37 ± 0.00	2.78 ± 0.00	63.52 ± 0.30	74.20 ± 0.62	82.50 ± 0.35	89.97 ± 0.35
25	4.39 ± 0.00	38.62 ± 0.00	77.24 ± 0.00	91.46 ± 0.00	1.70 ± 0.00	74.03 ± 0.01	83.97 ± 0.05	90.95 ± 0.04	96.26 ± 0.03
50	3.99 ± 0.00	41.87 ± 0.00	82.52 ± 0.00	92.68 ± 0.00	1.50 ± 0.01	79.90 ± 0.02	87.85 ± 0.02	93.12 ± 0.00	97.37 ± 0.00

dataset can still surpass self-supervised and supervised state-of-the-art pre-training techniques like ImageNet (which has one million images) when image and annotation availability is constrained.

## 6 Conclusions

Our research introduces a novel application of DDPMs for anatomical landmark detection in X-ray images, addressing the persistent challenge of limited annotated data in medical image analysis. This work bridges the gap between the established potential of diffusion models in medical imaging and the critical need for label-efficient methods in landmark localization.

We demonstrate that our DDPM-based self-supervised pre-training method consistently outperforms supervised ImageNet pre-training, traditional state-of-the-art self-supervised approaches (MoCoV3, SimCLRv2, DINO), and the YOLO framework in few-shot learning scenarios across Chest, Cephalometric, and Hand X-ray datasets. The performance gains are particularly significant in low-data regimes, with substantial MRE reductions and SDR improvements. Notably, our method maintains its effectiveness when pre-trained on one in-domain dataset and fine-tuned on smaller, distinct datasets, simulating real-world scenarios with limited data availability. This robustness suggests broad applicability across various medical imaging tasks and datasets.

Our work not only addresses the critical issue of data scarcity but also contributes to the ongoing discussion on effective pre-training strategies in medical image analysis. By showing the efficacy of DDPMs in this context, we aim to open new avenues for research into efficient and robust landmark detection methods, potentially accelerating progress in automated diagnosis systems.

## References

- [1] Bulat Ibragimov and Tomaž Vrtovec. Landmark-based statistical shape representations. In *Statistical Shape and Deformation Analysis*, pages 89–113. Elsevier, 2017.
- [2] James McCouat, Irina Voiculescu, and Siôn Glyn-Jones. Automatically diagnosing HIP conditions from x-rays using landmark detection. In *18th IEEE International Symposium on Biomedical Imaging, ISBI 2021, Nice, France, April 13-16, 2021*, pages 179–182. IEEE, 2021.
- [3] Minkyung Lee, Minyoung Chung, and Yeong-Gil Shin. Cephalometric landmark detection via global and local encoders and patch-wise attentions. *Neurocomputing*, 470:182–189, 2022.
- [4] C. A. Edwards, A. Goyal, A. E. Rusheen, A. Z. Kouzani, and K. H. Lee. Deepnavnet: Automated landmark localization for neuronavigation. *Frontiers in Neuroscience*, 15:670287, 2021.
- [5] S. Suganyadevi, V. Seethalakshmi, and K. Balasamy. A review on deep learning in medical image analysis. *Int. J. Multimed. Inf. Retr.*, 11(1):19–38, 2022.
- [6] Erik Meijering. Deep learning in bioimaging. *Computational and Structural Biotechnology Journal*, 18:2301–2313, 2020.
- [7] H Zhu, Q Yao, L Xiao, and SK Zhou. Learning to localize cross-anatomy landmarks in x-ray images with a universal model. *BME Front.*, 2022:9765095, Jun 2022.
- [8] Heqin Zhu, Qingsong Yao, Li Xiao, and S. Kevin Zhou. You only learn once: Universal anatomical landmark detection. In Marleen de Bruijne, Philippe C. Cattin, Stéphane Cotin, Nicolas Padoy, Stefanie Speidel, Yefeng Zheng, and Caroline Essert, editors, *Medical Image Computing and Computer Assisted Intervention - MICCAI 2021 - 24th International Conference, Strasbourg, France, September 27 - October 1, 2021, Proceedings, Part V*, volume 12905 of *Lecture Notes in Computer Science*, pages 85–95. Springer, 2021.

- [9] Roberto Di Via, Matteo Santacesaria, Francesca Odone, and Vito Paolo Pastore. Is in-domain data beneficial in transfer learning for landmarks detection in x-ray images? *CoRR*, abs/2403.01470, 2024.
- [10] Yankai Jiang, Yiming Li, Xinyue Wang, Yubo Tao, Jun Lin, and Hai Lin. Cephalformer: Incorporating global structure constraint into visual features for general cephalometric landmark detection. In Linwei Wang, Qi Dou, P. Thomas Fletcher, Stefanie Speidel, and Shuo Li, editors, *Medical Image Computing and Computer Assisted Intervention - MICCAI 2022 - 25th International Conference, Singapore, September 18-22, 2022, Proceedings, Part III*, volume 13433 of *Lecture Notes in Computer Science*, pages 227–237. Springer, 2022.
- [11] Zhiwei Wang, Jinxin Lv, Yunqiao Yang, Yuanhuai Liang, Yi Lin, Qiang Li, Xin Li, and Xin Yang. Accurate scoliosis vertebral landmark localization on x-ray images via shape-constrained multi-stage cascaded cnns. *CoRR*, abs/2206.02087, 2022.
- [12] Connor Elkhill, Scott LeBeau, Brooke French, and Antonio R. Porras. Graph convolutional network with probabilistic spatial regression: Application to craniofacial landmark detection from 3d photogrammetry. In Linwei Wang, Qi Dou, P. Thomas Fletcher, Stefanie Speidel, and Shuo Li, editors, *Medical Image Computing and Computer Assisted Intervention - MICCAI 2022 - 25th International Conference, Singapore, September 18-22, 2022, Proceedings, Part III*, volume 13433 of *Lecture Notes in Computer Science*, pages 574–583. Springer, 2022.
- [13] Qingsong Yao, Zecheng He, Hu Han, and S. Kevin Zhou. Miss the point: Targeted adversarial attack on multiple landmark detection. In Anne L. Martel, Purang Abolmaesumi, Danail Stoyanov, Diana Mateus, Maria A. Zuluaga, S. Kevin Zhou, Daniel Racoceanu, and Leo Joskowicz, editors, *Medical Image Computing and Computer Assisted Intervention - MICCAI 2020 - 23rd International Conference, Lima, Peru, October 4-8, 2020, Proceedings, Part IV*, volume 12264 of *Lecture Notes in Computer Science*, pages 692–702. Springer, 2020.
- [14] Thanaporn Viriyasaranon, Serie Ma, and Jang Hwan Choi. Anatomical landmark detection using a multiresolution learning approach with a hybrid transformer-cnn model. In Hayit Greenspan, Anant Madabhushi, Parvin Mousavi, Septimiu Salcudean, James Duncan, Tanveer F. Syeda-Mahmood, and Russell H. Taylor, editors, *Medical Image Computing and Computer Assisted Intervention - MICCAI 2023 - 26th International Conference, Vancouver, BC, Canada, October 8-12, 2023, Proceedings, Part VI*, volume 14225 of *Lecture Notes in Computer Science*, pages 433–443. Springer, 2023.
- [15] Akhil Kasturi, Ali Vosoughi, Nathan Hadjiyski, Larry Stockmaster, William J Sehnert, and Axel Wismüller. Anatomical landmark detection in chest x-ray images using transformer-based networks. In *Medical Imaging 2024: Computer-Aided Diagnosis*, volume 12927, pages 647–660. SPIE, 2024.
- [16] Heqin Zhu, Quan Quan, Qingsong Yao, Zaiyi Liu, and S. Kevin Zhou. UOD: universal one-shot detection of anatomical landmarks. In Hayit Greenspan, Anant Madabhushi, Parvin Mousavi, Septimiu Salcudean, James Duncan, Tanveer F. Syeda-Mahmood, and Russell H. Taylor, editors, *Medical Image Computing and Computer Assisted Intervention - MICCAI 2023 - 26th International Conference, Vancouver, BC, Canada, October 8-12, 2023, Proceedings, Part I*, volume 14220 of *Lecture Notes in Computer Science*, pages 24–34. Springer, 2023.
- [17] Hee E. Kim, Alejandro Cosa-Linan, Nandhini Santhanam, Mahboubeh Jannesari, Máté E. Maros, and Thomas Ganslandt. Transfer learning for medical image classification: a literature review. *BMC Medical Imaging*, 22(1):69, 2022.
- [18] L. Alzubaidi, M. Al-Amidie, A. Al-Asadi, A. J. Humaidi, O. Al-Shamma, M. A. Fadhel, J. Zhang, J. Santamaría, and Y. Duan. Novel transfer learning approach for medical imaging with limited labeled data. *Cancers*, 13(7):1590, 2021.
- [19] Yiting Xie and David Richmond. Pre-training on grayscale imagenet improves medical image classification. In Laura Leal-Taixé and Stefan Roth, editors, *Computer Vision - ECCV 2018 Workshops - Munich, Germany, September 8-14, 2018, Proceedings, Part VI*, volume 11134 of *Lecture Notes in Computer Science*, pages 476–484. Springer, 2018.
- [20] Larbi Touijer, Vito Paolo Pastore, and Francesca Odone. Food image classification: The benefit of in-domain transfer learning. In *International Conference on Image Analysis and Processing*, pages 259–269. Springer, 2023.
- [21] Xinlei Chen, Saining Xie, and Kaiming He. An empirical study of training self-supervised vision transformers. In *2021 IEEE/CVF International Conference on Computer Vision, ICCV 2021, Montreal, QC, Canada, October 10-17, 2021*, pages 9620–9629. IEEE, 2021.
- [22] Ting Chen, Simon Kornblith, Kevin Swersky, Mohammad Norouzi, and Geoffrey E. Hinton. Big self-supervised models are strong semi-supervised learners. In Hugo Larochelle, Marc’Aurelio Ranzato, Raia Hadsell, Maria-Florina Balcan, and Hsuan-Tien Lin, editors, *Advances in Neural Information Processing Systems 33: Annual Conference on Neural Information Processing Systems 2020, NeurIPS 2020, December 6-12, 2020, virtual*, 2020.

- [23] Mathilde Caron, Hugo Touvron, Ishan Misra, Hervé Jégou, Julien Mairal, Piotr Bojanowski, and Armand Joulin. Emerging properties in self-supervised vision transformers. In *2021 IEEE/CVF International Conference on Computer Vision, ICCV 2021, Montreal, QC, Canada, October 10-17, 2021*, pages 9630–9640. IEEE, 2021.
- [24] Prafulla Dhariwal and Alexander Quinn Nichol. Diffusion models beat gans on image synthesis. In Marc’Aurelio Ranzato, Alina Beygelzimer, Yann N. Dauphin, Percy Liang, and Jennifer Wortman Vaughan, editors, *Advances in Neural Information Processing Systems 34: Annual Conference on Neural Information Processing Systems 2021, NeurIPS 2021, December 6-14, 2021, virtual*, pages 8780–8794, 2021.
- [25] Gustav Müller-Franzes, Jan Moritz Niehues, Firas Khader, Soroosh Tayebi Arasteh, Christoph Haarburger, Christiane Kuhl, Tianci Wang, Tianyu Han, Sven Nebelung, Jakob Nikolas Kather, and Daniel Truhn. Diffusion probabilistic models beat gans on medical images. *CoRR*, abs/2212.07501, 2022.
- [26] Quan Quan, Qingsong Yao, Jun Li, and S. Kevin Zhou. Which images to label for few-shot medical landmark detection? In *IEEE/CVF Conference on Computer Vision and Pattern Recognition, CVPR 2022, New Orleans, LA, USA, June 18-24, 2022*, pages 20574–20584. IEEE, 2022.
- [27] Jonathan Ho, Ajay Jain, and Pieter Abbeel. Denoising diffusion probabilistic models. In Hugo Larochelle, Marc’Aurelio Ranzato, Raia Hadsell, Maria-Florina Balcan, and Hsuan-Tien Lin, editors, *Advances in Neural Information Processing Systems 33: Annual Conference on Neural Information Processing Systems 2020, NeurIPS 2020, December 6-12, 2020, virtual*, 2020.
- [28] Sema Candemir, Stefan Jaeger, Kannappan Palaniappan, Jonathan P. Musco, Rahul K. Singh, Zhiyun Xue, Alexandros Karargyris, Sameer K. Antani, George R. Thoma, and Clement J. McDonald. Lung segmentation in chest radiographs using anatomical atlases with nonrigid registration. *IEEE Trans. Medical Imaging*, 33(2):577–590, 2014.
- [29] Ching-Wei Wang, Cheng-Ta Huang, Jia-Hong Lee, Chung-Hsing Li, Sheng-Wei Chang, Ming-Jhih Siao, Tat-Ming Lai, Bulat Ibragimov, Tomaz Vrtovec, Olaf Ronneberger, Philipp Fischer, Timothy F. Cootes, and Claudia Lindner. A benchmark for comparison of dental radiography analysis algorithms. *Medical Image Anal.*, 31:63–76, 2016.
- [30] Arkadiusz Gertych, Aifeng Zhang, James W. Sayre, Sylwia Pospiech-Kurkowska, and H. K. Huang. Bone age assessment of children using a digital hand atlas. *Comput. Medical Imaging Graph.*, 31(4-5):322–331, 2007.
- [31] Christian Payer, Darko Stern, Horst Bischof, and Martin Urschler. Integrating spatial configuration into heatmap regression based cnns for landmark localization. *Medical Image Anal.*, 54:207–219, 2019.
- [32] Zihao Yin, Ping Gong, Chunyu Wang, Yizhou Yu, and Yizhou Wang. One-shot medical landmark localization by edge-guided transform and noisy landmark refinement. In Shai Avidan, Gabriel J. Brostow, Moustapha Cissé, Giovanni Maria Farinella, and Tal Hassner, editors, *Computer Vision - ECCV 2022 - 17th European Conference, Tel Aviv, Israel, October 23-27, 2022, Proceedings, Part XXI*, volume 13681 of *Lecture Notes in Computer Science*, pages 473–489. Springer, 2022.
- [33] Nikolaos Giakoumoglou and Paschalis Giakoumoglou. Pyssl: A pytorch implementation of self-supervised learning (ssl) methods. <https://github.com/giakou4/pyssl>, 2023.
- [34] Pavel Iakubovskii. Segmentation models pytorch. [https://github.com/qubvel/segmentation\\_models.pytorch](https://github.com/qubvel/segmentation_models.pytorch), 2019.
- [35] James McCouat and Irina Voiculescu. Contour-hugging heatmaps for landmark detection. In *IEEE/CVF Conference on Computer Vision and Pattern Recognition, CVPR 2022, New Orleans, LA, USA, June 18-24, 2022*, pages 20565–20573. IEEE, 2022.